J. Fluid Mech. (2026), *vol.* 1031, A14, doi:10.1017/jfm.2026.11288

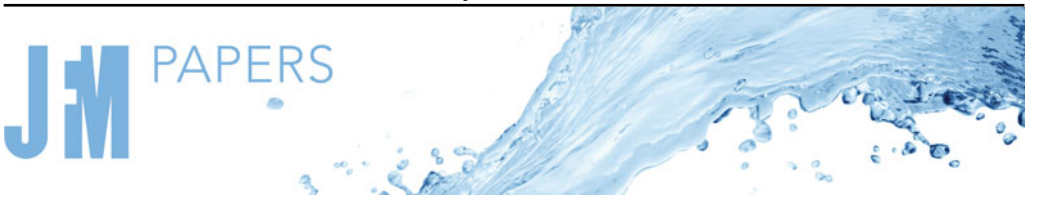

Hydrodynamic origin of friction between suspended rough particles

Jake Minten[1] **and Bhargav Rallabandi**[1]

[1]Department of Mechanical Engineering, University of California, Riverside, CA 92521, USA

Corresponding author: Bhargav Rallabandi, bhargav@engr.ucr.edu

(Received 19 August 2025; revised 23 January 2026; accepted 1 February 2026)

Tangential interactions between particles play a central role in suspension rheology. We show that surface roughness significantly enhances the strength of hydrodynamic interactions between closely separated particles in relative sliding motion. Using numerical solutions of the lubrication equation, we show that tangential forces due to sliding motion between rough spheres scale inversely with the separation distance, as opposed to the weaker logarithmic scaling for smooth spheres. A fully analytic theory identifies these features as the consequence of asperity-scale squeeze flows, quantitatively recovering the numerical results. These singular hydrodynamic forces are associated with similarly singular torques. The need to resolve the hydrodynamic singularity couples the particles' rotation to their translation, and forces them to roll without slip, recovering a kinematic constraint that is central to understanding dense suspension rheology. Despite their purely hydrodynamic origin and occurring without contact, these features resemble several aspects of rolling and sliding contact friction.

Key words: colloids, lubrication theory

1. Introduction

The flow of particulate suspensions is central to a range of industrial, geophysical and biological processes. Suspensions of rigid colloids exhibit complex rheological behaviours, including discontinuous shear-thickening (DST), characterised by an orders-of-magnitude increase in viscosity with shear rate above a critical particle volume fraction (Guazzelli & Pouliquen 2018; Ness, Seto & Mari 2022). This is a direct consequence of inter-particle interactions, particularly those that constrain rotational and translational degrees of freedom of the particles (Wyart & Cates 2014; Hsiao *et al.* 2017*b*; Singh *et al.* 2020). However, classical lubrication theory for smooth spherical particles predicts forces

and torques that are too weak to enforce these constraints (Foss & Brady 2000; Melrose & Ball 2004).

Meanwhile, a growing body of experimental evidence implicates surface roughness as the main cause for particle-scale kinematic constraints and DST (Hsiao *et al.* 2017*a*,*b*; Hsu *et al.* 2018; Schroyen *et al.* 2019; Yanagishima *et al.* 2021; Ilhan, Mugele & Duits 2022; Pradeep, Wessel & Hsiao 2022; Ilhan *et al.* 2022). One potential consequence of this roughness is for particles to make physical contact at high volume fractions, marking a transition from lubrication to frictional behaviour (Lemaire *et al.* 2023). Theoretical models of pairwise rough-particle interactions have typically combined hydrodynamic and contact interactions (da Cunha & Hinch 1996; Zhao, Galvin & Davis 2002; Zhao & Davis 2003; Davis *et al.* 2003; Blanc, Peters & Lemaire 2011). Suspension-scale simulations adopting the frictional-interaction framework have reproduced several experimentally observed rheological features including DST (Seto *et al.* 2013; Fernandez *et al.* 2013; Wyart & Cates 2014; Mari *et al.* 2014; Gallier *et al.* 2014; Townsend & Wilson 2017). Simulations of suspension rheology have also studied the effects of contact elasticity (More & Ardekani 2020*a*,*b*, 2021) and a velocity-dependent coefficient of friction (Ruiz-Lopez *et al.* 2023). Recent work (Dumont *et al.* 2025) has shown that DST can occur even for dry grains, and can be modelled with a non-Coulombic friction law.

By contrast, Stokesian hydrodynamic simulations of suspensions (Jamali & Brady 2019) that explicitly account for the rough-particle geometry have recovered rheological signatures without invoking contact friction. Wang, Jamali & Brady (2020) implement a phenomenological modification of lubrication forces to model roughness in simulations of suspensions of otherwise smooth spheres and also recover rheology resembling DST without contact forces. This suggests a need to better understand the implications of roughness on hydrodynamic interactions between particles even before they come into contact (Ness *et al.* 2022). Systematic efforts to understand hydrodynamic features at the asperity scale (and implications thereof on particle-scale forces) have focused either on small roughness amplitude, or on the interaction of a single rough surface with a smooth one (Kurzthaler *et al.* 2020; Chase, Kurzthaler & Stone 2022; Yariv *et al.* 2024; Kargar-Estahbanati & Rallabandi 2025). These studies have identified modified hydrodynamic interaction laws, but do not reproduce the strong rotational constraints necessary to explain suspension rheology.

Here, we develop a rigorous thin-film theory for interactions of suspended rough particles close to contact. In particular, we focus on situations where both surfaces are rough, as is the case in most practical situations, allowing asperities on opposing surfaces to interact hydrodynamically with each other. We show that hydrodynamic features at the scale of roughness asperities lead to large point-like tangential forces and torques that greatly exceed their smooth counterparts, as well as those that arise when a rough surface interacts with a smooth one. The forces grow as the inverse of the separation distance $1/d$, in contrast with the weak $\log d$ scaling for smooth spheres. Even in the absence of physical contact, these hydrodynamic singularities enforce a rolling constraint on the particles, exhibiting characteristics reminiscent of dry contact friction.

2. Set-up

We consider the near-contact hydrodynamics of two spherical particles of radius a, whose surfaces are decorated with small roughness asperities (bumps); see figure 1(*a*). The particle surfaces are separated by a nominal 'macroscopic' gap D, while the 'microscopic' gap d – defined as the minimum separation between the asperities – can be much smaller. Hydrodynamic features are highly localised to the small gaps between opposing asperities,

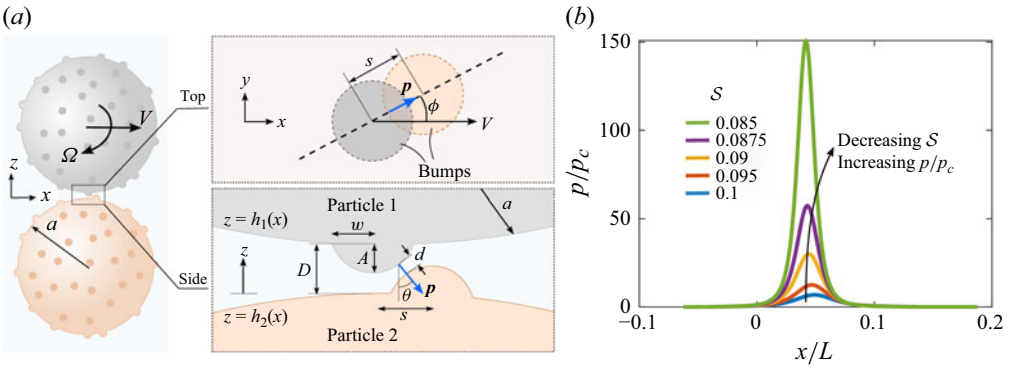

Figure 1. (*a*) Two spherical particles of radius a, with asperities of width w and amplitude A, rotate and translate relative to each other. The microscale separation d between asperities can be much smaller than the nominal separation D between the particles, leading to singular hydrodynamic forces in the approach to contact. (*b*) Pressure profile in the gap at $y = 0$, showing a sharp spike as the bumps approach contact (decreasing $\mathcal{S}$).

so we focus on a single pair of asperities (one per particle). The bumps are treated as spherical caps with amplitude A, radial width w, a relative orientation angle ϕ, and a centre-to-centre distance s in the plane of the gap. The amplitude is small relative to the particle radius, but can be comparable to the gap D.

We allow the top particle (particle 1) to translate with velocity $V\boldsymbol{e}_x$ and rotate with angular velocity $\Omega\boldsymbol{e}_y$, while keeping the lower particle (particle 2) fixed; more general kinematics will be treated elsewhere. We consider small gaps and gentle bump profiles, i.e. $D \ll a$ and $A \ll w$, providing necessary and sufficient conditions for lubrication theory, but will place no restriction on A/D. Under these geometric conditions, all spherical surfaces can be approximated as paraboloidal. Thus, the rough-particle surfaces are encoded by $z = h_{1,2}(\boldsymbol{x})$, defined in (A1), where $\boldsymbol{x} = (x, y)$ represents locations in the plane of the gap; see figure 1(*a*).

Rather than follow the trajectory of the asperities through time, we characterise the system in configuration space. Defining the gap profile $h(\boldsymbol{x}) = h_1(\boldsymbol{x}) - h_2(\boldsymbol{x})$ and twice the mean gap surface $\overline{h}(\boldsymbol{x}) = h_1(\boldsymbol{x}) + h_2(\boldsymbol{x})$, the pressure $p(\boldsymbol{x})$ is governed by the Reynolds equation (see Appendix A):

$$\boldsymbol{\nabla} \cdot \left[\frac{h^3}{12\mu} \boldsymbol{\nabla} p + \frac{\overline{h}}{2} \left(V - a\Omega \right) \boldsymbol{e}_x \right] + \Omega x = 0, \tag{2.1}$$

where μ is the viscosity of the fluid and $\boldsymbol{\nabla}$ is the gradient in the xy-plane. We non-dimensionalise by scales characteristic of the smooth limit: distances across the gap by D, horizontal distances by $L = \sqrt{2aD}$, and the pressure by $p_c = \mu V L / D^2$. The rescaled problem involves the dimensionless amplitude $\mathcal{A} = A/D$ and width $\mathcal{W} = w/L$ of the asperities, their relative in-plane orientation ϕ and separation $\mathcal{S} = s/L$, which together set the dimensionless gap $\delta = d/D$. We numerically solve the rescaled form of (2.1) for the pressure distribution, and then integrate the stresses of the flow to obtain forces and torques exerted by the flow on the particles (see Appendix B).

To aid the discussion, we temporarily suppress rotation and focus on bumps oriented head-on ($\phi = 0$); both constraints will be relaxed later. We first discuss the horizontal force F_x, which we decompose into a combination of smooth $F_{x,S}$ and rough $F_{x,R} = F_x - F_{x,S}$ contributions. Including Stokes drag, the smooth contribution is

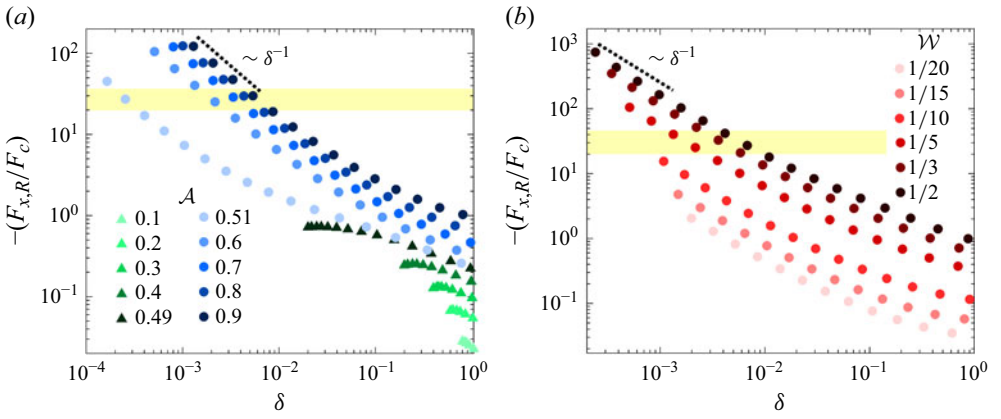

Figure 2. Dimensionless horizontal force (rough contribution) versus gap height δ for a pair of opposing asperities. The force $F_{x,R}$ scales as δ^{-1} for $\mathcal{A} > 1/2$, and exceeds the smooth contribution (shaded region). Results are given at (*a*) fixed $\mathcal{W} = 1/5$ for a range of $\mathcal{A}$, (*b*) fixed $\mathcal{A} = 0.6$ for a range of $\mathcal{W}$. The force increases with both $\mathcal{A}$ and $\mathcal{W}$.

(Jeffrey & Onishi 1984)

$$F_{x,S} \approx 6\pi F_c \left[\frac{1}{6}\log\left(\frac{a}{D}\right) + 1\right], \tag{2.2}$$

where $F_c = \mu a V$ is the characteristic force scale on the particle. The logarithmic term is due to smooth-particle lubrication and depends only weakly on the gap (i.e. it is only approximately as large as Stokes drag even for D/a as small as 10^{-3}). The rough contribution to the force, which is our focus, depends on the inter-bump separation δ, which we control by varying the in-plane separation $\mathcal{S}$ between the bumps. The bump on particle 1 is centred for simplicity, but this is non-essential for our discussion.

From numerical solutions, we find that the pressure is highly localised in the gap between the asperities (figure 1*b*). It is also much greater than the scale expected for smooth spheres. The pressure grows in magnitude and becomes further localised as the bumps are brought closer together by decreasing $\mathcal{S}$, which decreases the gap width δ.

These localised pressure features correlate with increased horizontal forces, unlike for smooth particles where the horizontal force is largely caused by shear. Increasing either the amplitude or width of the asperities increases $F_{x,R}$ (figure 2). When $\mathcal{A} < 0.5$ (or $A < D/2$, cf. figure 1*a*), all horizontal positions $\mathcal{S}$ are accessible, and the rough contribution to the force remains negligible relative to the smooth case (figure 2*a*). This behaviour changes qualitatively as soon as $\mathcal{A}$ exceeds 0.5. Now, each asperity occupies more than half the nominal gap width, restricting the available configuration space (limiting the range of $\mathcal{S}$). The asperities are now in a state of impending contact under a tangential sliding of the particles (figure 1*a*). In this regime, δ approaches zero as the bumps come horizontally closer, leading to a sharp increase in force. Even for a single pair of asperities, this rough hydrodynamic force can overwhelm the smooth-sphere sliding lubrication force (shaded regions in figure 2). The numerical results suggest that the force diverges as a power-law δ^{-1}, which lies in stark contrast with the much weaker (logarithmic) smooth contribution. This scaling is consistent with a squeeze flow between the asperities due to tangential sliding of the particles, suggested in previous work (Wang *et al.* 2020). It is therefore of interest to understand how the prefactors of this scaling behaviour depend on the geometry of the particles and the asperities.

3. Theory

To understand the numerical results we zoom into a 'local' region characterising the gap between the asperities (see the side view of figure 1*a*). In this region, the asperities themselves appear as spheres of radius $b = a\kappa/(1+\kappa)$, separated by a gap d, where $\kappa = w^2/(2Aa) = \mathcal{W}^2/\mathcal{A}$ is a measure of the bump's curvature relative to that of the particle. The hydrodynamics of the inter-bump gap are governed by a horizontal length scale $\ell = \sqrt{2bd} \propto w\sqrt{d/A}$, which becomes much smaller than both w and L as the bumps approach contact. We exploit this separation of scales to isolate the bumps from the rest of the geometry, and invoke lubrication theory once more, this time in the thin film between the two spherical bump surfaces in relative translation. The force on bump 1 in the local configuration takes the form

$$\boldsymbol{F} = -\mu b\left[R_n \boldsymbol{p}\boldsymbol{p} + R_t\,(\boldsymbol{I} - \boldsymbol{p}\boldsymbol{p})\right]\cdot(V\boldsymbol{e}_x), \tag{3.1}$$

where R_n and R_t are dimensionless resistance coefficients for normal and tangential motion between bumps, respectively, $\boldsymbol{I}$ is the identity matrix, and $\boldsymbol{p} = \sin\theta\cos\phi\,\boldsymbol{e}_x + \sin\theta\sin\phi\,\boldsymbol{e}_y - \cos\theta\,\boldsymbol{e}_z$ is the unit vector which connects the centres of the two bumps and is normal to their surfaces (figure 1*a*). Also, ϕ is the orientation angle introduced earlier, while θ is a polar angle that depends on the relative position of the bumps.

When the distance between asperities is small ($d \ll b$), the resistances are

$$R_n = \frac{3\pi}{2}\frac{b}{d}, \quad R_t = \frac{\pi}{2}\log\left(1 + \frac{A}{d}\right). \tag{3.2}$$

The normal resistance R_n is a well-known result (Cox 1974), whereas the tangential resistance R_t is slightly modified from the usual result as the outer cutoff of the logarithm is set by the bumps' width w rather than their radius of curvature b (Appendix C). Importantly, R_n scales as d^{-1} and is associated with a squeeze flow between bumps, while R_t, which is due to shear, grows weakly as $\log d^{-1}$.

Substituting (3.2) into (3.1) leads to general expressions for the force components:

$$F_{x,R} = -\mu bV\left[(R_n - R_t)\sin^2\theta\cos^2\phi + R_t\right], \tag{3.3a}$$

$$F_{y,R} = -\mu bV(R_n - R_t)\sin^2\theta\sin\phi\cos\phi, \tag{3.3b}$$

$$F_{z,R} = \mu bV(R_n - R_t)\sin\theta\cos\theta\cos\phi. \tag{3.3c}$$

The polar angle θ is a function of the microscopic geometry ($\mathcal{A}$, $\mathcal{W}$ and $\mathcal{S}$) and thus depends implicitly on δ. Under a small-angle approximation consistent with the thin-film geometry, we find (Appendix A)

$$\sin\theta \approx \sqrt{\frac{(2A - D + d)(1+\kappa)}{a\kappa(1+2\kappa)}}. \tag{3.4}$$

Substituting this result into (3.3*a*) yields

$$F_{x,R} = -\mu aV\mathcal{K}\left[\frac{3\pi}{2}\left(\frac{2\mathcal{A}-1}{\delta} + 1\right)\cos^2\phi + R_t\right]. \tag{3.5}$$

Here, we have defined the dimensionless geometric quantity

$$\mathcal{K} = \frac{\kappa}{(1+\kappa)(1+2\kappa)} = \frac{(b/a)(1-b/a)}{(1+b/a)}, \tag{3.6}$$

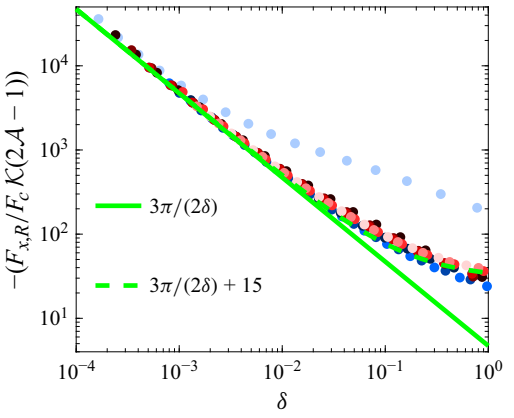

Figure 3. Horizontal force $F_{x,R}$ rescaled by the theoretically predicted scale $F_c\mathcal{K}(2\mathcal{A}-1)$, plotted against δ. Symbols are data from figure 2, which collapse into the theoretical prediction $3\pi/(2\delta)$ for small δ (solid line) for all $\mathcal{A}$ and $\mathcal{W}$, without fitting parameters. The collapse persists for larger δ, and is captured by adding a subdominant empirical constant $c = 15$ to the theoretical prediction (dashed curve).

which depends on the ratio of the bump to the particle curvatures; note that $\mathcal{K} \sim \kappa = w^2/(2Aa)$ for small κ. The tangential rough contribution R_t is much smaller than even the smooth case (Appendix C) so we neglect it for the remainder of the discussion.

The analytic theory (3.5) fully reproduces the features of the numerical results in figure 2. When $\mathcal{A} < 1/2$, the bumps can pass over each other, so the more singular R_n contribution vanishes at closest approach ($\theta = 0$, where $\delta = 1 - 2\mathcal{A}$) and only the smaller logarithmic R_t contribution survives. By contrast, when $\mathcal{A} > 1/2$ each bump is taller than half the nominal gap width, so a sliding motion of the particles decreases their separation between their surfaces down to zero. That is, sliding motion of the particles for $\mathcal{A} > 1/2$ necessitates a squeeze flow between asperities, generating a δ^{-1} hydrodynamic force that resists contact. Despite its small prefactor, the δ^{-1} singularity from a single bump-pair quickly overwhelms the combined 'smooth' Stokes drag and lubrication forces on the rest of the sphere (shaded region in figure 2). An estimate of this crossover for typical experiments in made in § 5.

We quantitatively test the theory in the singular regime $\mathcal{A} > 1/2$. As the bumps approach contact, (3.5) reduces to

$$F_{x,R} \sim -F_c \frac{3\pi\mathcal{K}}{2}\frac{(2\mathcal{A}-1)}{\delta}\cos^2\phi, \quad \mathcal{A} > 1/2. \tag{3.7}$$

We use this result to rescale the numerical results of figure 2 by the scaling factor $(2\mathcal{A}-1)\mathcal{K}$. The rescaled data collapse onto the theoretical prediction $3\pi/(2\delta)$ for small δ, without adjustable parameters (figure 3). Unexpectedly, this collapse persists even when δ is not small, and is described rather well by a universal curve $-(3\pi/(2\delta) + c)$, where we find the subdominant term $c \approx 15$ from a fit.

Thus, the introduction of roughness with small but finite amplitude A such that $D/2 \leqslant A \ll a$ leads to a singular perturbation of the hydrodynamic resistance. While the smooth contribution scales as $\log(\delta^{-1})$, the rough contribution scales more singularly as δ^{-1}, albeit with a prefactor that is smaller by a factor of (b/a). The rough contribution is essentially 'switched on' when $A > D/2$ ($\mathcal{A} > 1/2$), which is the regime of impending contact between asperities under a sliding of the particles. This threshold is observed clearly in the numerical results, and emerges naturally in the theory. In a situation with multiple bumps, the threshold $A > D/2$ corresponds to configurations where particles can

interlock, which has been identified as important to DST in past work (Hsu *et al.* 2018). However, while the interactions of interlocking particles are normally thought to be driven by contact friction, we see that similar interactions can arise due to hydrodynamics alone in the approach to contact. This can occur only when both surfaces are rough; if one of the surfaces is smooth, only the subdominant R_t term survives since there is no geometric mechanism to generate a squeeze flow. We refer the reader to Yariv *et al.* (2024) for a two-dimensional analogue with a single rough surface, and Kargar-Estahbanati & Rallabandi (2025) for a treatment that also includes elastic deformation.

The theory provides a natural framework for arbitrary orientations ϕ between asperities. The predicted ϕ dependences in (3.3) are confirmed by our numerical solutions (Appendix C). At fixed ϕ, all three force components depend on R_n, diverging as δ^{-1} for $\mathcal{A} > 1/2$. However, not all three components are equally important on average. Any physically realisable system of rough particles will involve an ensemble of pairwise bump interactions with different orientations at any instant of time. If bumps are distributed isotropically on the particles, all orientations $\phi \in [0, 2\pi)$ are realised with equal probability. Then, averaging (3.3) over ϕ leads to the average force per pair of opposing bumps,

$$\langle F_{x,R} \rangle = -F_c \frac{3\pi \mathcal{K}}{4} \frac{(2\mathcal{A}-1)}{\delta}, \quad \langle F_{y,R} \rangle = \langle F_{z,R} \rangle = 0, \tag{3.8}$$

valid for $\mathcal{A} > 1/2$ (observe that the average force is half of the maximum). Forces in the direction of motion (x) survive the averaging since F_x always opposes particle motion regardless of orientation, while the other components average out to zero, due to orientational symmetry at the asperity scale. Thus, the configurational averaging retrieves the macroscopic Stokesian symmetry of the two-sphere system. We note that different averages may be more or less appropriate depending on the constraints of the problem (e.g. prescribed force versus prescribed motion). We expect different averaging methods to lead to similar results up to $O(1)$ prefactors.

4. Coupling of rotation and translation

We now generalise to include rotation $\Omega \boldsymbol{e}_y$ in addition to translation $V\boldsymbol{e}_x$, focusing on how these degrees of freedom are coupled by roughness. We also keep track of the torque on the particle, only the y-component of which (T_y) is relevant in the average sense for isotropically distributed roughness. For the same reason, we neglect vertical translation, which will not, on average, couple to horizontal translation or rotation due to symmetry. Under this configurationally averaged setting, the mobility relation connecting a tangential force and torque due to tangential sliding and rotation of particle 1 is

$$\begin{bmatrix} F_x \\ T_y \end{bmatrix} = -\mu a \begin{bmatrix} \mathcal{R}_{FV} & a\mathcal{R}_{F\Omega} \\ a\mathcal{R}_{TV} & a^2\mathcal{R}_{T\Omega} \end{bmatrix} \cdot \begin{bmatrix} V \\ \Omega \end{bmatrix}, \tag{4.1}$$

where the $\mathcal{R}_{ij}$ are dimensionless resistance coefficients (note that $\mathcal{R}_{F\Omega} = \mathcal{R}_{TV}$ due to symmetry).

The $\mathcal{R}_{FV}$ coefficient relates the force to the particle velocity, and is identical to the quantity $F_{x,R}/F_c$ in figures 2 and 3, where we had set $\Omega = 0$. To understand the rough contributions to the other coefficients we revisit the local theory. Including particle rotation merely modifies the approach velocity of the asperities in (3.1) from $V\boldsymbol{e}_x$ to $(V - a\Omega)\boldsymbol{e}_x$, which carries through to all subsequent theoretical results for the force. The rough contribution to the torque on particle 1 is $\boldsymbol{T}_R = \int \boldsymbol{r} \times \boldsymbol{n} \cdot \boldsymbol{\sigma}_R \mathrm{d}S$, where $\boldsymbol{\sigma}_R$ is the stress due to roughness, $\boldsymbol{n}$ is the normal vector, and $\boldsymbol{r}$ is the moment arm connecting the

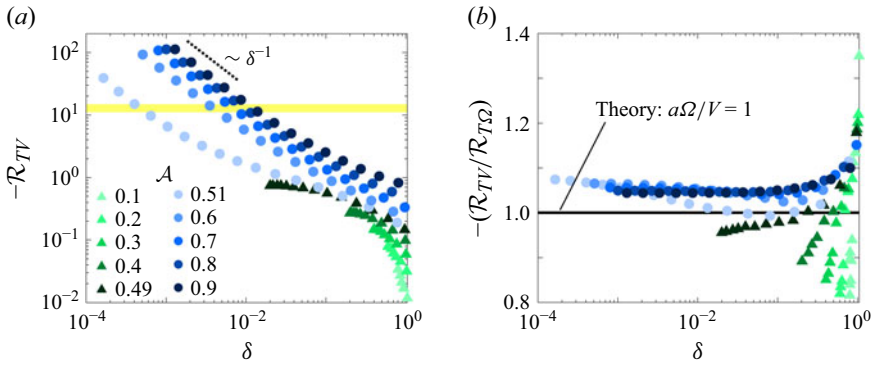

Figure 4. (*a*) Resistance coefficient $\mathcal{R}_{TV}$ (showing rough contributions only) versus δ, for fixed $\mathcal{W} = 1/5$ and various $\mathcal{A}$. The data are virtually identical to those in figure 2(*a*). Shaded region indicates a typical range for smooth particles for $D/a \in (10^{-3}, 10^{-1})$. (*b*) Ratio of resistance coefficients $\mathcal{R}_{TV}/\mathcal{R}_{T\Omega} = a\Omega/V$ versus δ. For all $\mathcal{A}$ and all δ, the ratio is always close to 1, indicating strong rotation–translation coupling.

centre of the particle to a point on its surface S. As shown in figure 1(*b*) and predicted by the theory, stresses are localised to a small region of length $\ell \ll L$ surrounding the minimum separation of the bumps. Within this region, the moment arm is effectively the constant vector $\boldsymbol{r}_c$ connecting the centre of particle 1 to the point of minimum separation. The torque is therefore $\boldsymbol{T}_R \approx \boldsymbol{r}_c \times \boldsymbol{F}_R$, where $\boldsymbol{F}_R = \int \boldsymbol{n} \cdot \boldsymbol{\sigma}_R \mathrm{d}S$ is the rough contribution to the force discussed previously. This cross product does not vanish even though $\boldsymbol{F}_R$ is largely a normal force (directed along $\boldsymbol{p}$) since $\boldsymbol{p}$ is misaligned with the moment arm $\boldsymbol{r}_c$ (this is not the case for smooth spheres). Then, the torque on the particle is simply a consequence of the rough force acting at an effective point of contact. We thus conclude that all four resistance coefficients are identical up to sign:

$$\mathcal{R}_{FV} = -\mathcal{R}_{F\Omega} = -\mathcal{R}_{TV} = \mathcal{R}_{T\Omega} = \frac{3\pi\mathcal{K}}{2}\frac{(2\mathcal{A}-1)}{\delta}\cos^2\phi, \quad (\mathcal{A} > 1/2). \tag{4.2}$$

Our numerical calculations quantitatively corroborate these predictions. The torque due to translation, $\mathcal{R}_{TV}$, is virtually identical to $\mathcal{R}_{FV}$ (compare figure 4*a* with figure 2*a*), diverging as δ^{-1} for $\mathcal{A} > 1/2$ and exceeding the torque on a smooth particle. If particle 1 is torque-free, its rotation and translation are coupled according to

$$\frac{\Omega a}{V} = -\frac{\mathcal{R}_{TV}}{\mathcal{R}_{T\Omega}}. \tag{4.3}$$

For small gaps, the torque from roughness dominates that from the rest of the two-particle geometry, and this ratio approaches unity according to the theory (4.2), corresponding to $\Omega a/V \approx 1$. This prediction is in agreement with the numerical results (figure 4*b*), and corresponds precisely to vanishing relative surface velocity $V - a\Omega$. This hydrodynamic 'pure-rolling' condition recovers the kinematic constraint of classical dry rolling friction. It is interesting to note that the rolling condition persists across the range of δ, even when the resistance coefficients are not particularly large (note the short range of the vertical axis in figure 4*b*). This is due primarily to the localisation of the force on the sub-asperity scale, which allows it to behave similarly to a point-like contact force. We contrast this with the case of smooth particles, where the coupling is negligible (Cox 1974; Hsiao *et al.* 2017*b*), i.e. torque-free smooth particles experience a very weak (logarithmic) coupling that decays rapidly with D. The roughness-induced torque dominates over the smooth contribution close to contact (i.e. when $A > D/2$), and so we expect rotation and translation to be strongly coupled in this regime. This coupling is insensitive to the geometric details of the

roughness, and stems from the generation of large forces and localisation of the stresses on sub-asperity length scales in the interlocking regime.

The constraining of rotational modes to translational ones has been identified as a central piece in the rheology of dense suspensions. Past work has interpreted it as a kinematic constraint that occurs on contact, akin to the rotation of interlocked gears (see e.g. Singh *et al.* 2020). The present work provides an alternative interpretation of this feature. If the particles did not roll when slid against each other, there would be relative motion between asperities in near-contact. This would generate squeeze flows, producing d^{-1} singular forces and torques. The need to relieve this impending hydrodynamic singularity as asperities approach (or pull apart) underpins the hydrodynamic interpretation of the rolling constraint.

5. Discussion and conclusions

We have shown that local hydrodynamic interactions between asperities lead generically to a strong singular behaviour of tangential forces and torques on rough particles near contact. From (3.8) to (4.2), the configurationally averaged rough contribution to the force, $\langle F_{x,R}\rangle$, and torque, $\langle T_{y,R}\rangle$,

$$\langle F_{x,R}\rangle = -a^{-1}\langle T_{y,R}\rangle = -6\pi\mu a(V - a\Omega)\frac{(b/a)}{8}\frac{(2A - D)}{d}. \tag{5.1}$$

Even for a single pair of bumps, these forces can exceed hydrodynamic forces between smooth particles, and occur when the nominal separation between particles falls below twice the roughness amplitude. On the scale of the particles, the roughness-induced hydrodynamic features manifest as localised forces that act at an effective point of contact. These point-like forces generate torque, which also greatly exceeds its smooth counterpart. Together, these large forces and torques tightly constrain rotation to translation.

From (5.1), we see that the mean rough force contribution exceeds the smooth one (assuming $D = O(A)$), when $d \gtrsim A(b/a)/8$. For a typical experiment with colloidal particles of radius $a = 1\,\mu\text{m}$ and asperities with $A \sim b = 100\,\text{nm}$, the rough force from a single pair of asperities becomes comparable to Stokes drag when the separation $d \lesssim 15\,\text{nm}$. The same force, relative to Stokes drag, would be generated for somewhat larger d for realistic micron-sized particles, which have multiple asperities covering their surface. By contrast, the contribution from classical (smooth) lubrication (2.2) is only approximately 40 % of Stokes drag for the same parameters. For larger particles or larger asperities, the rough contribution would exceed the smooth one for proportionately greater d. The coupling between rotation and translation, which stems from the localisation of stresses at the asperity scale, would likely persist for even greater d, as is suggested by figure 4(*b*).

The present theory is agnostic to the length scale of the particles or the asperities, provided that continuum hydrodynamics and low-Reynolds-number conditions apply. The continuum approximation remains valid as long as the Knudsen number $Kn = \lambda/d$ is small, where λ is the mean free path of the fluid molecules. In the case of rough micron-sized particles described earlier (with $d \sim 15\,\text{nm}$, for which the rough force is comparable to Stokes drag), and assuming mean free path $\lambda \sim 0.1\,\text{nm}$ typical of liquids, the Knudsen number is $Kn \lesssim 0.01$. We therefore expect the present continuum theory to apply to typical colloidal suspensions used in experiments. The restrictions on δ are weaker for larger particles or asperities.

On the one hand, the forces discussed here share many similarities with frictional contact forces: they are point-like, and occur below a threshold separation of the order

of the roughness amplitude. Macroscopically, this threshold can be viewed as an effective contact distance at which these forces become 'activated'. On the other hand, they are purely hydrodynamic and scale with particle velocity, becoming singular as the inverse of the microscopic surface separation distance d. These hydrodynamic forces and torques occur precisely to avoid an impending hard contact between asperities. Thus, rough hydrodynamic forces form a bridge between smooth hydrodynamic interactions and frictional contact forces. It is interesting to observe that the present hydrodynamic forces are kinematically reversible at the asperity scale. By contrast, contact-based forces are not reversible beyond molecular length scales (separating asperities does not lead to a contact force). The implications of this asperity-scale reversibility on the motion of particles with a distribution of surface asperities remains to be explored.

For nanoscopic gaps, it may also be necessary to account for other kinds of surface forces, e.g. Derjaguin-Landau-Verwey-Overbeek or van der Waals forces, which could ultimately drive particles to physical contact. It may also be important to consider the effects of compressibility, piezo-viscosity or non-continuum effects in nanometric gaps. While the present theory is expected to become quantitatively modified in situations where these effects are important, the qualitative features identified here should remain applicable. That is, the need to squeeze fluid out from between approaching roughness asperities would lead to significant resistance to particle motion.

Our findings thus form a fundamental hydrodynamic basis for near-contact interactions in suspensions of rough particles. Roughness produces a singular perturbation to classical lubrication theory, leading to large hydrodynamic resistances in near-contact configurations. These modified resistances would be important – and relatively straightforward – to include in simulations of dense suspension flows. The same principles would apply to other lubricated systems involving rough surfaces, including those with engineered surface textures in tribological, biological and robotic applications.

Acknowledgements. The authors thank A. Greaney, H. Stone and E. Yariv for insightful conversations.

Funding. J.M. acknowledges support from the US Department of Education through award P200A210080.

Declaration of interests. The authors report no conflict of interest.

Appendix A. Geometry and lubrication equation

We consider two particles with a single asperity each. Under a long-wave theory consistent with lubrication flow, the spheres and bumps are approximated as paraboloids. We thus define the surfaces of the particles by

$$z = h_1(\boldsymbol{x}) = D + \frac{|\boldsymbol{x}|^2}{2a} - \beta_1(\boldsymbol{x}), \tag{A1a}$$

$$z = h_2(\boldsymbol{x}) = -\frac{|\boldsymbol{x}|^2}{2a} + \beta_2(\boldsymbol{x}). \tag{A1b}$$

The functions $\beta_i(\boldsymbol{x})$ define the bumps according to

$$\beta_i(\boldsymbol{x}) = \begin{cases} A\left(1 - \dfrac{|\boldsymbol{x} - \boldsymbol{s}_i|^2}{w^2}\right) & \text{for} \quad |\boldsymbol{x} - \boldsymbol{s}_i| \leqslant w, \\ 0 & \text{for} \quad |\boldsymbol{x} - \boldsymbol{s}_i| > w, \end{cases} \tag{A2}$$

where $\boldsymbol{s}_i$ are the locations of the bumps in the xy-plane. We choose $\boldsymbol{s}_1 = \boldsymbol{0}$ and $\boldsymbol{s}_2 = s(\cos\phi\, \boldsymbol{e}_x + \sin\phi\, \boldsymbol{e}_y)$.

Particle 1 translates with velocity $V\boldsymbol{e}_x$ and rotates with angular velocity $\Omega\boldsymbol{e}_y$, while particle 2 is stationary. We split the velocity $\boldsymbol{v}$ into an in-plane component $\boldsymbol{u}$ and an out-of-plane component v_z, writing $\boldsymbol{v} = \boldsymbol{u} + v_z\boldsymbol{e}_z$. Under the usual lubrication approximation, the in-plane velocity is

$$\boldsymbol{u} = \frac{\boldsymbol{\nabla} p}{2\mu}(z - h_1(\boldsymbol{x}))(z - h_2(\boldsymbol{x})) + (V - a\Omega)\frac{z - h_2(\boldsymbol{x})}{h_1(\boldsymbol{x}) - h_2(\boldsymbol{x})}\boldsymbol{e}_x. \tag{A3}$$

Integrating the continuity equation ($\boldsymbol{\nabla}\cdot\boldsymbol{u} + \partial_z v_z = 0$) over the gap yields (2.1).

To relate the polar angle θ to the separation d, which enters (3.3), we analyse the near-contact geometry. Without loss of generality, we orient the bumps along x and set $y = 0$ ($\phi = 0$). Setting $\partial h/\partial x = 0$ identifies the location of minimum separation as $x_m = s/[2(1+\kappa)]$. The minimum separation distance is then $d = h(x_m)$, which we rearrange to obtain the s at minimum separation: $s = 2\sqrt{\kappa(1+\kappa)(2A - D + d)a/(1+2\kappa)}$. Finally, we approximate $\sin\theta = \partial h_1/\partial x|_{x_m} = \partial h_2/\partial x|_{x_m}$ to arrive at (3.4).

Appendix B. Numerical methods

We use two nested grids to solve the problem, one localised near the point of closest approach, encompassing the bumps, and another that includes a larger portion of the particles beyond the bumps (the global grid). The global (local) grids are defined on a square of side L_g (L_l), each with $n+1$ grid points along a dimension. We set $L_g = 20$ throughout. To resolve the full bump structure, we target $L_f = 4\mathcal{W}$ and round up to the nearest integer multiple of a global grid cell (whose side has length L_g/n). The local grid is therefore defined within the bounds of the global grid and resolves the solution on the scale of the asperities.

We non-dimensionalise (2.1) and discretise it using central finite differences on both grids. We solve the discretised system numerically on both grids for pressure using a Gauss–Seidel iteration with multi-grid acceleration (Press 2007, p. 1066). Let us denote the boundary of the local grid by B. We first relax the problem by a step on the global grid, fixing the pressure data at B. During this global iteration we 'mask' the region enclosed by B (which is occupied by the local grid) to avoid solving the problem there. Then, we relax the solution on the local grid by a step, utilising the pressure gradient from the coarse iteration as a boundary condition on B. Iterating back and forth between the two grids achieves convergence while guaranteeing continuity of the pressure and its gradient; continuity of second-order derivatives is enforced by (2.1). This method allows us to simultaneously resolve the rapid pressure variations between the bumps and the global lubrication problem at reduced computational effort. The effects of the bumps decay rapidly away from the point of minimum separation where the gap widens. We therefore use the smooth-sphere solution to enforce boundary conditions at the edge of the computational domain, greatly suppressing domain-size effects in the computation. For the particular kinematics considered here, the smooth-sphere pressure is identically zero.

To compute the rough contribution to the forces, we split the corresponding integrals by adding and subtracting the tractions for the smooth problem. For example, the horizontal force $F_x = \int_S \sigma_{nx}\,\mathrm{d}S$ (here, σ_{nx} is the x-component of the surface traction and $\mathrm{d}S$ is the elemental area in the gap) is split as

$$F_x = \underbrace{\int_S \sigma_{nx}^S\,\mathrm{d}S}_{F_{x,S}} + \underbrace{\int_S \left(\sigma_{nx} - \sigma_{nx}^S\right)\mathrm{d}S}_{F_{x,R}}. \tag{B1}$$

n	$F_{x,R}/F_c$ ($\delta = 0.0151$)	$F_{x,R}/F_c$ ($\delta = 0.00149$)
2^5	-1.99661	-5.0282
2^6	-0.52136	-1.0374
2^7	-0.61562	-5.5035
2^8	-0.61594	-5.2150
2^9	-0.61591	-5.2158
2^{10}	-0.61596	-5.2159

Table 1. Grid-independence study: computed value of the rescaled horizontal force $F_{x,R}/F_c$ for different grid resolutions n and two different δ for the non-rotating case with $\mathcal{A} = 0.6$, $\mathcal{W} = 0.1$.

The superscript S indicates the smooth contribution, and is known analytically (Jeffrey & Onishi 1984). The first integral is the known smooth contribution to the force, while the second is the rough contribution and is calculated numerically. The rough integrand is localised around the origin, so the integral converges rapidly independent of domain size. The results of a grid-independence study for two different δ are shown in table 1. We typically use $n = 2^9$ for the results reported in the main text.

Appendix C. Resistance coefficients

C.1. *Tangential resistance*

To compute R_t, we consider the local flow between tangentially translating bumps. The pressure in this configuration is identically zero. Using dimensional quantities for clarity, the traction on particle 1 in the direction of motion is due to shear and is given by $-\mu V/h$, where $h = d + |\tilde{\boldsymbol{x}}|^2/b$ is the gap between two bumps, where $\tilde{\boldsymbol{x}}$ is a local coordinate vector in the gap centred at the point of minimum separation. Integrating over the local plane of the gap and comparing with (3.2) gives $R_t = \pi \log(1 + r_\infty^2/(bd)) + c_1$, r_∞ being an outer radial cutoff distance and c_1 being a constant that is independent of d but possibly depending on other geometric quantities. While the outer cutoff for isolated spheres is their radius (Cox 1974), the cutoff for the truncated bumps is of the order of their radial width w. Noting that $b \sim \kappa a = w^2/(2A)$, up to higher orders in κ, we thus find

$$R_t = \pi \log\left(1 + \frac{\mathcal{A}}{\delta}\right) + c_1. \tag{C1}$$

To test this prediction, we consider $\phi = \pi/2$, where the force is given solely by R_t; see (3.3). Numerical force calculations in this configuration agree very well with the analytic prediction without fitting parameters, up to the small additive matching constant c_1 (figure 5). The R_t contribution remains much smaller than the Stokes drag even for quite small δ.

C.2. *Dependence on orientation*

To test the ϕ-dependence of (3.3), we control the bump height and width as with the head-on ($\phi = 0$) case, but vary the angle ϕ at a fixed separation $\mathcal{S}$ (fixing δ). For $\mathcal{A} > 1/2$, (3.3) reduces to

$$F_{x,R}^{th} = F_w \cos^2\phi, \quad F_{y,R}^{th} = F_w \frac{\sin 2\phi}{2} \quad \text{and} \quad F_{z,R}^{th} = F_v \cos\phi, \tag{C2}$$

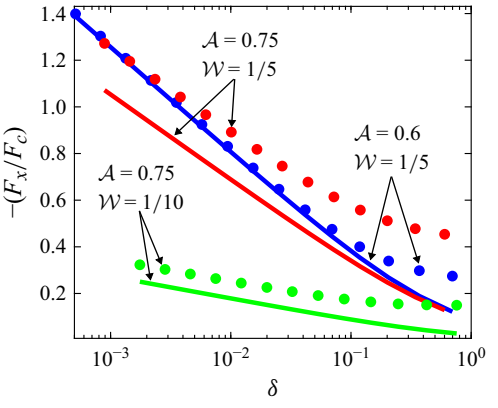

Figure 5. Dimensionless force along x when $\phi = \pi/2$ from numerical calculations (symbols) plotted alongside analytic predictions (curves), which are due to tangential resistance R_t. The predictions are offset from the numerical by an $O(1)$ additive constant associated with the logarithm.

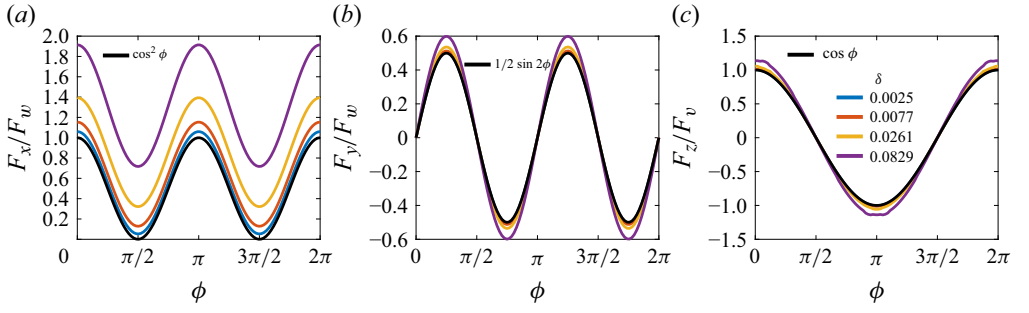

Figure 6. Variation of rescaled forces with the inter-bump orientation ϕ at $\mathcal{A} = 0.6$ and $\mathcal{W} = 1/5$ for different δ, showing (*a*) F_x/F_w, (*b*) F_y/F_w and (*c*) F_z/F_v. Analytic predictions from (C2) for small δ are indicated as black curves.

where

$$F_w = -F_c \frac{3\pi}{2} \frac{\kappa(2\mathcal{A}-1)}{(1+\kappa)(1+2\kappa)} \frac{1}{\delta} \quad \text{and} \quad F_v = \frac{\mu V L^3}{D^2} \left(\frac{\kappa}{2(1+\kappa)}\right)^{3/2} \left(\frac{2\mathcal{A}-1}{1+2\kappa}\right)^{1/2} \frac{1}{\delta}. \tag{C3}$$

Rescaling F_x and F_y by F_w, and F_z by F_v, we plot the numerical results against the analytic prediction of (C2) in figure 6, finding agreement at small δ without fit parameters. Note that F_x curves are offset from the prediction due to R_t. The offset shrinks as $\delta \to 0$.

References

Blanc, F., Peters, F. & Lemaire, E. 2011 Experimental signature of the pair trajectories of rough spheres in the shear-induced microstructure in noncolloidal suspensions. *Phys. Rev. Lett.* **107** (20), 208302.

Chase, D.L., Kurzthaler, C. & Stone, H.A. 2022 Hydrodynamically induced helical particle drift due to patterned surfaces. *Proc. Acad. Natl Sci. USA* **119** (31), e2202082119.

Cox, R. 1974 The motion of suspended particles almost in contact. *Intl J. Multiphase Flow* **1** (2), 343–371.

da Cunha, F.R. & Hinch, E.J. 1996 Shear-induced dispersion in a dilute suspension of rough spheres. *J. Fluid Mech.* **309**, 211–223.

Davis, R.H., Zhao, Y., Galvin, K.P. & Wilson, H.J. 2003 Solid–solid contacts due to surface roughness and their effects on suspension behaviour. *Phil. Trans. R. Soc. Lond. A* **361** (1806), 871–894.

DUMONT, D., ROCHA, F.M., NICOLAS, M. & POULIQUEN, O. 2025 Discontinuous shear thickening in dry granular materials induced by non-coulombian friction. *Phys. Rev. Fluids* **10**, 064302.
FERNANDEZ, N., MANI, R., RINALDI, D., KADAU, D., MOSQUET, M., LOMBOIS-BURGER, H., CAYER-BARRIOZ, J., HERRMANN, H.J., SPENCER, N.D. & ISA, L. 2013 Microscopic mechanism for shear thickening of non-Brownian suspensions. *Phys. Rev. Lett.* **111** (10), 108301.
FOSS, D.R. & BRADY, J.F. 2000 Structure, diffusion and rheology of Brownian suspensions by Stokesian Dynamics simulation. *J. Fluid Mech.* **407**, 167–200.
GALLIER, S., LEMAIRE, E., PETERS, F. & LOBRY, L. 2014 Rheology of sheared suspensions of rough frictional particles. *J. Fluid Mech.* **757**, 514–549.
GUAZZELLI, É. & POULIQUEN, O. 2018 Rheology of dense granular suspensions. *J. Fluid Mech.* **852**, P1.
HSIAO, L.C., JAMALI, S., GLYNOS, E., GREEN, P.F., LARSON, R.G. & SOLOMON, M.J. 2017*a* Rheological state diagrams for rough colloids in shear flow. *Phys. Rev. Lett.* **119** (15), 158001.
HSIAO, L.C., SAHA-DALAL, I., LARSON, R.G. & SOLOMON, M.J. 2017*b* Translational and rotational dynamics in dense suspensions of smooth and rough colloids. *Soft Matt.* **13** (48), 9229–9236.
HSU, C.-P., RAMAKRISHNA, S.N., ZANINI, M., SPENCER, N.D. & ISA, L. 2018 Roughness-dependent tribology effects on discontinuous shear thickening. *Proc. Natl Acad. Sci. USA* **115** (20), 5117–5122.
ILHAN, B., MUGELE, F. & DUITS, M.H. 2022 Roughness induced rotational slowdown near the colloidal glass transition. *J. Colloid Interface Sci.* **607**, 1709–1716.
JAMALI, S. & BRADY, J.F. 2019 Alternative frictional model for discontinuous shear thickening of dense suspensions: hydrodynamics. *Phys. Rev. Lett.* **123** (13), 138002.
JEFFREY, D.J. & ONISHI, Y. 1984 Calculation of the resistance and mobility functions for two unequal rigid spheres in low-Reynolds-number flow. *J. Fluid Mech.* **139**, 261–290.
KARGAR-ESTAHBANATI, A. & RALLABANDI, B. 2025 Non-monotonic frictional behavior in the lubricated sliding of soft patterned surfaces. *Soft Matt.* **21** (3), 448–457.
KURZTHALER, C., ZHU, L., PAHLAVAN, A.A. & STONE, H.A. 2020 Particle motion nearby rough surfaces. *Phys. Rev. Fluids* **5** (8), 082101.
LEMAIRE, E., BLANC, F., CLAUDET, C., GALLIER, S., LOBRY, L. & PETERS, F. 2023 Rheology of non-Brownian suspensions: a rough contact story. *Rheol. Acta* **62** (5), 253–268.
MARI, R., SETO, R., MORRIS, J.F. & DENN, M.M. 2014 Shear thickening, frictionless and frictional rheologies in non-Brownian suspensions. *J. Rheol.* **58** (6), 1693–1724.
MELROSE, J.R. & BALL, R.C.2004 Continuous shear thickening transitions in model concentrated colloids – the role of interparticle forces. *J. Rheol.* **48** (5), 937–960.
MORE, R. & ARDEKANI, A. 2020*a* Roughness induced shear thickening in frictional non-brownian suspensions: a numerical study. *J. Rheol.* **64** (2), 283–297.
MORE, R.V. & ARDEKANI, A.M. 2020*b* Effect of roughness on the rheology of concentrated non-Brownian suspensions: a numerical study. *J. Rheol.* **64** (1), 67–80.
MORE, R.V. & ARDEKANI, A.M. 2021 Unifying disparate rate-dependent rheological regimes in non-Brownian suspensions. *Phys. Rev. E* **103**, 062610.
NESS, C., SETO, R. & MARI, R. 2022 The physics of dense suspensions. *Annu. Rev. Condens. Matter Phys.* **13** (2022), 97–117.
PRADEEP, S., WESSEL, A. & HSIAO, L.C. 2022 Hydrodynamic origin for the suspension viscoelasticity of rough colloids. *J. Rheol.* **66** (5), 895–906.
PRESS, W.H. 2007 *Numerical Recipes 3rd Edition: The Art of Scientific Computing*. Cambridge University Press.
RUIZ-LOPEZ, J.A., PRASANNA KUMAR, S.S., VAZQUEZ-QUESADA, A., DE VICENTE, J. & ELLERO, M. 2023 Tribological variable-friction coefficient models for the simulation of dense suspensions of rough polydisperse particles. *J. Rheol.* **67** (2), 541–558.
SCHROYEN, B., HSU, C.-P., ISA, L., VAN PUYVELDE, P. & VERMANT, J. 2019 Stress contributions in colloidal suspensions: the smooth, the rough, and the hairy. *Phys. Rev. Lett.* **122** (21), 218001.
SETO, R., MARI, R., MORRIS, J.F. & DENN, M.M. 2013 Discontinuous shear thickening of frictional hard-sphere suspensions. *Phys. Rev. Lett.* **111** (21), 218301.
SINGH, A., NESS, C., SETO, R., DE PABLO, J.J. & JAEGER, H.M. 2020 Shear thickening and jamming of dense suspensions: the 'roll' of friction. *Phys. Rev. Lett.* **124** (24), 248005.
TOWNSEND, A.K. & WILSON, H.J. 2017 Frictional shear thickening in suspensions: the effect of rigid asperities. *Phys. Fluids* **29** (12), 121607.
WANG, M., JAMALI, S. & BRADY, J.F. 2020 A hydrodynamic model for discontinuous shear-thickening in dense suspensions. *J. Rheol.* **64** (2), 379–394.
WYART, M. & CATES, M.E. 2014 Discontinuous shear thickening without inertia in dense non-Brownian suspensions. *Phys. Rev. Lett.* **112** (9), 098302.

YANAGISHIMA, T., LIU, Y., TANAKA, H. & DULLENS, R.P.A. 2021 Particle-level visualization of hydrodynamic and frictional couplings in dense suspensions of spherical colloids. *Phys. Rev. X* **11** (2), 021056.

YARIV, E., BRANDÃO, R., WOOD, D.K., SZAFRANIEC, H., HIGGINS, J.M., BAZAZI, P., PEARCE, P. & STONE, H.A. 2024 Hydrodynamic interactions between rough surfaces. *Phys. Rev. Fluids* **9** (3), L032301.

ZHAO, Y. & DAVIS, R.H. 2003 Interaction of sedimenting spheres with multiple surface roughness scales. *J. Fluid Mech.* **492**, 101–129.

ZHAO, Y., GALVIN, K.P. & DAVIS, R.H. 2002 Motion of a sphere down a rough plane in a viscous fluid. *Intl J. Multiphase Flow* **28** (11), 1787–1800.